The Meteoritical Society

Meteoritics & Planetary Science 44, Nr 6, 787–804 (2009)
Abstract available online at http://meteoritics.org

Refractory inclusions and aluminum-rich chondrules in Sayh al Uhaymir 290 CH chondrite: Petrography and mineralogy

Aicheng ZHANG[1, 2] and Weibiao HSU[1, 3*]

[1]Laboratory for Astrochemistry and Planetary Sciences, Lunar and Planetary Science Center, Purple Mountain Observatory, Chinese Academy of Sciences, 2 West Beijing Road, Nanjing 21008, China
[2]State Key Laboratory for Mineral Deposits Research, Nanjing University, Nanjing 210093, China
[3]Faculty of Earth Science, China University of Geosciences, Wuhan 430074, China
[*]Corresponding author. E-mail: wbxu@pmo.ac.cn

(Received 24 September 2008; revision accepted 07 March 2009)

Abstract–Here we report the petrography, mineralogy, and bulk compositions of Ca,Al-rich inclusions (CAIs), amoeboid olivine aggregate (AOA), and Al-rich chondrules (ARCs) in Sayh al Uhaymir (SaU) 290 CH chondrite. Eighty-two CAIs (0.1% of the section surface area) were found. They are hibonite-rich (9%), grossite-rich (18%), melilite ± spinel-rich (48%), fassaite ± spinel-rich (15%), and fassaite-anorthite-rich (10%) refractory inclusions. Most CAIs are rounded in shape and small in size (average = 40 μm). They are more refractory than those of other groups of chondrites. CAIs in SaU 290 might have experienced higher peak heating temperatures, which could be due to the formation region closer to the center of protoplanetary disk or have formed earlier than those of other groups of chondrites. In SaU 290, refractory inclusions with a layered texture could have formed by gas-solid condensation from the solar nebula and those with an igneous texture could have crystallized from melt droplets or experienced subsequent melting of pre-existing condensates from the solar nebula. One refractory inclusion represents an evaporation product of pre-existing refractory solid on the basis of its layered texture and melting temperature of constituting minerals. Only one AOA is observed (75 μm across). It consists of olivine, Al-diopside, anorthite, and minor spinel with a layered texture. CAIs and AOA show no significant low-temperature aqueous alteration. ARCs in SaU 290 consist of diopside, forsterite, anorthite, Al-enstatite, spinel, and mesostasis or glass. They can be divided into diopside-rich, Al-enstatite-rich, glass-rich, and anorthite-rich chondrules. Bulk compositions of most ARCs are consistent with a mixture origin of CAIs and ferromagnesian chondrules. Anorthite and Al-enstatite do not coexist in a given ARC, implying a kinetic effect on their formation.

INTRODUCTION

CH chondrites are a group of primitive carbonaceous chondrites (Bischoff et al. 1993). Typical members include Allan Hills (ALH) 85085, Acfer 182, and Northwest Africa (NWA) 739 and 770. They are characterized by: 1) abundant FeNi-metal (~20 vol%) grains; 2) small chondrule and Ca,Al-rich inclusion (CAI) sizes (<100 μm); 3) dominance of cryptocrystalline chondrules; 4) lack of matrix (<5 vol%) and presence of heavily hydrated lithic clasts; 5) large depletions in bulk volatile and moderately volatile element abundances (Krot et al. 2003; Scott 2007). Currently, this group consists of 20 meteorites, some of which are paired, such as Acfer 182, 207, and 214, and all of which are classified as type 3 (Meteoritical Bulletin Database).

CAIs in CH chondrites have three distinctive characteristics: 1) smaller sizes than those in other chondrites (e.g., CV3, CO3); 2) high abundances of grossite, which is relatively rare in other chondrites; 3) lack of evidence of thermal and aqueous metamorphism on their parent bodies (Bischoff et al. 1993; Kimura et al. 1993; Brearley and Jones 1998; Krot et al. 2002b, 2006a). The latter two characteristics suggest that CAIs in CH chondrites are more refractory and primitive than those in other chondrites (e.g., CV3 and CO3). However, some investigators (MacPherson et al. 1989; Kimura et al. 1993; Weber et al. 1995; Krot et al. 2008) found that most grossite- and hibonite-bearing CAIs lack excess of ^{26}Mg, the decay product of short-lived radionuclide ^{26}Al. Furthermore, CH CAIs have a bimodal distribution of oxygen isotopic compositions (Sahijpal et al. 1999; Krot et al. 2008) whereas oxygen isotopic compositions are homogeneous within individual CAI (Kimura et al. 1993; Sahijpal et al. 1999). These characteristics are different from those of CAIs found

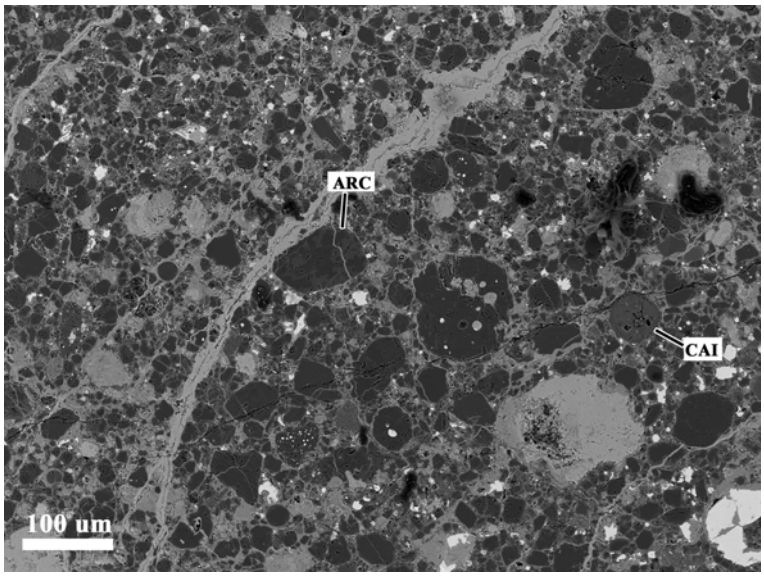

Fig. 1. Back-scattered electron (BSE) image of an area of SaU 290 showing abundant mineral and polymineralic fragments, chondrule fragments, chondrules, Al-rich chondrule (ARC), Ca,Al-rich inclusions (CAI), and metals embedded in a light-grey, Fe-rich matrix.

in other primitive carbonaceous chondrites (e.g., CV3). Recently, Krot et al. (2008) suggested that ^{16}O-rich CAIs without excess of ^{26}Mg in CH chondrites probably formed prior to the injection of ^{26}Al into the solar system. To better understand these unusual features (e.g., petrographic, mineralogical, and isotopic) of CAIs in CH chondrites, more detailed and systematic investigations are needed for CH chondrites.

Sayh al Uhaymir (SaU) 290 is a CH carbonaceous chondrite discovered from Oman in 2005 (Bartoschewitz et al. 2005). This meteorite was once classified as an anomalous E-chondrite based on its noble gas composition (Park et al. 2005). It was reclassified as a CH chondrite based on its petrology, bulk chemistry, oxygen isotopes, and characteristic heavy δ^{15}N value (Bartoschewitz et al. 2005; Murty et al. 2007). In this study, we report petrography and mineralogy of refractory inclusions and Al-rich chondrules in SaU 290, compare them with counterparts from other carbonaceous chondrites, and discuss possible implications for their formation history.

ANALYTICAL METHODS

The polished thin section of SaU 290 used in this study has an area of ~2.3 cm^2. Petrographic observation was carried out on a Hitachi 3400N II scanning electron microscope (SEM) with the back-scattered electron (BSE) mode. Qualitative analyses of mineral phases or glasses in the refractory inclusions and Al-rich chondrules were made with energy dispersive spectroscopy (EDS). Quantitative chemical analyses were carried out with JEOL 8100 electron microprobes (EMP) operating at an acceleration voltage of 15 kV and a probe current of 20 nA. Commercial standards from the SPI Company and National Bureau of Standards are used for quantitative analyses. All the data were reduced with the ZAF routine.

Bulk compositions of refractory inclusions and Al-rich chondrules were obtained by using analytical mode of irregularly outlined materials of PointID Navigator in the Oxford EDS system (INCA software). The energy dispersive spectrometer scans a selected area and the outputs are average results of elements in the selected area. Natural olivine, diopside, albite, and ilmenite were used as standards for elements Si, Mg, Fe, Ca, Al, and Ti with 100 s counting time. Analytical conditions of samples are the same to the standards. Before measuring bulk compositions of refractory inclusions and Al-rich chondrules, system reproducibility of these elements was established through repeated analyses of the same areas of standards. Although this technique has a relatively low precision compared to a wave dispersive spectrometer, the results appear reasonable given the inherent limitations of two-dimensional analyses (Hezel 2007).

RESULTS

Petrography and Mineralogy

SaU 290 exhibits a breccia texture with abundant chondrules, minerals, fragments, and metal grains (Fig. 1). The abundance of CAIs is very low (about 0.1% of the section area). Some dark inclusions with and without tiny magnetite framboids occur in variable sizes. Most metal grains are oxidized and some weathering veins occur across the thin section.

Ca, Al-Rich Inclusions and Amoeboid Olivine Aggregate

Eighty-two CAIs and one amoeboid olivine aggregate (AOA) were observed in the thin section. Size (diameter) distribution of these refractory inclusions is shown in Fig. 2. Most refractory inclusions are smaller than 80 μm and the average size is ~40 μm. CAIs are rounded or irregular in shape (Figs. 3–6). A few CAIs are monomineralic (e.g., melilite, spinel) but most are polymineralic. These CAIs can be grouped into hibonite-rich, grossite-rich, melilite±spinel-rich, fassaite±spinel-rich, and fassaite-anorthite-rich subgroups. Some CAIs might be a continuum among different types. For instance, a few inclusions have nearly equivalent abundances of grossite and hibonite (e.g., A0006 and A0007). Low-temperature secondary phases, such as nepheline, grossular, hedenbergite, andradite, and phyllosilicate minerals, were not observed in the CAIs.

Hibonite-rich CAIs (9% of the total), 40–55 μm in diameter, have rounded shapes (Fig. 3). They are hibonite-fassaite-melilite (A0020), hibonite-melilite±perovskite (A0068), hibonite-fassaite (A0053), and hibonite-spinel-melilite (A0022) CAIs. In these inclusions, hibonite occurs as euhedral laths and is surrounded by melilite or fassaite. A0020 shows a core-mantle texture with a hibonite-fassaite core and a hibonite-melilite rim. The core shows a digested outline (Fig. 3a). A0022 also has a core-mantle texture with a hibonite-spinel core surrounded by a thick melilite mantle (Fig. 3b); some small baddeleyite grains (<4 μm) also exist in this inclusion. In A0053, platy and granular hibonite grains are enclosed by fassaite, very similar to the hibonite-bearing micro-spherule (MUR7-228) from Murchison (Ireland et al. 1991) and the pyroxene-hibonite spherule (86) in Acfer 094 (Krot et al. 2004a). Fassaite in A0053 exhibits heterogeneity of brightness on the BSE image (Fig. 3c), corresponding to chemical variations of Al_2O_3 and TiO_2. Perovskite is absent in most hibonite-rich CAIs, but occurs in A0068.

Grossite-rich inclusions (18%) are 30–100 μm in size. Most of them are rounded or oval in shape and a few exhibit irregular outlines (Fig. 4). The grossite-rich inclusions show variable petrographic and mineralogical characteristics from inclusion to inclusion. Some grossite-rich inclusions consist of grossite, hibonite, and melilite with or without perovskite (Figs. 4a, 4b, and 4d). One oval inclusion (A0024) consists dominantly of grossite with two discontinued melilite-perovskite layers (Fig. 4c). Melilite grains in this inclusion are irregular. In two of the irregular-shaped inclusions, grossite is surrounded by a double-layered rim composed of spinel-hibonite-perovskite (inner layer) and diopside or melilite (outer layer) (A0046, Fig. 4e). Grossite also occurs with spinel and melilite. Spinel grains show digested outlines and are enclosed by melilite (Fig. 4f). Hibonite grains in grossite-rich inclusions have various occurrences (granular, columnar, acicular, and platy) among different grossite-rich inclusions (Figs. 4a, 4b, 4d, and 4e).

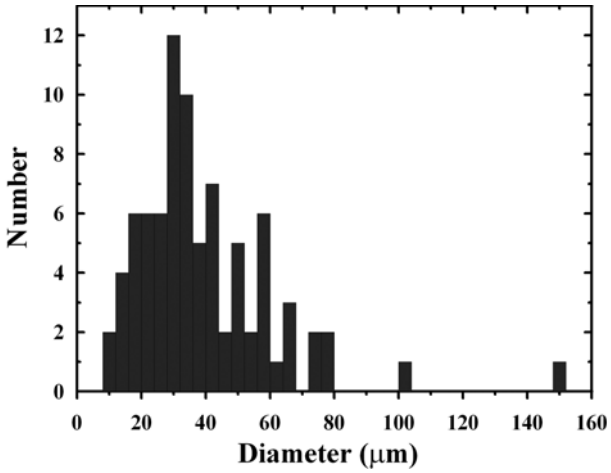

Fig. 2. Size (diameter) distribution of CAIs and AOA in SaU 290.

Melilite ± spinel-rich CAIs (48%), 30–150 μm in size, are rounded or irregular in shape (Fig. 5). Melilite-rich CAIs consist of melilite and spinel with variable modal abundances (from 100 vol% melilite to 84 vol% spinel +16 vol% melilite). One melilite-rich CAI (A0012) contains spinel-hibonite assemblage in the core (Fig. 5c). Some irregular perovskite grains are enclosed by melilite. In A0028, several irregular-shaped fassaite grains are included by melilite. Both fassaite and spinel grains in this inclusion exhibit digested boundaries. In a large inclusion (A0019), spinel is the predominant phase while irregular melilite grains exist in the interstices of spinel grains. Some monomineralic melilite inclusions are also observed.

Fassaite ± spinel-rich CAIs (15%), 20–100 μm in size, are rounded or irregular in shape. Most fassaite-rich CAIs are characterized by a spinel core and a fassaite mantle. A fassaite-rich CAI (A0013) also contains minor grains of anorthite, pyroxene, and forsterite (Fig. 6a). Some fassaite-rich CAIs contain irregular melilite and spinel in the interior. Spinel occurs as inclusions in melilite or layers between melilite and fassaite (Fig. 6b). One fassaite-rich CAI consists of Al-rich diopside and Sc-rich fassaite as the mantle and two Sc-,Ti-,Y-, and Zr-rich phases (ox1 and ox2) and Os-, Ir-dominant metal grains as the core (Fig. 6c).

Some fassaite-anorthite-rich CAIs (10%), 36–65 μm size, also exist in SaU 290. In these inclusions, irregular anorthite grains are embraced by fassaite, and minor forsterite grains exist at the rims of some of these inclusions. Irregular fine spinel grains are common in these inclusions. In one fassaite-anorthite-rich inclusion (A0082), a spinel-fassaite mineral assemblage with a digested outline is included by anorthite (Fig. 6d). The spinel-fassaite mineral assemblage could be a remnant of a CAI precursor.

Amoeboid olivine aggregates are rare in CH chondrites and only one irregular AOA (75 μm across) is observed in SaU 290. This aggregate consists of olivine, Al-diopside, and anorthite with a layered texture (Fig. 7). The AOA is similar

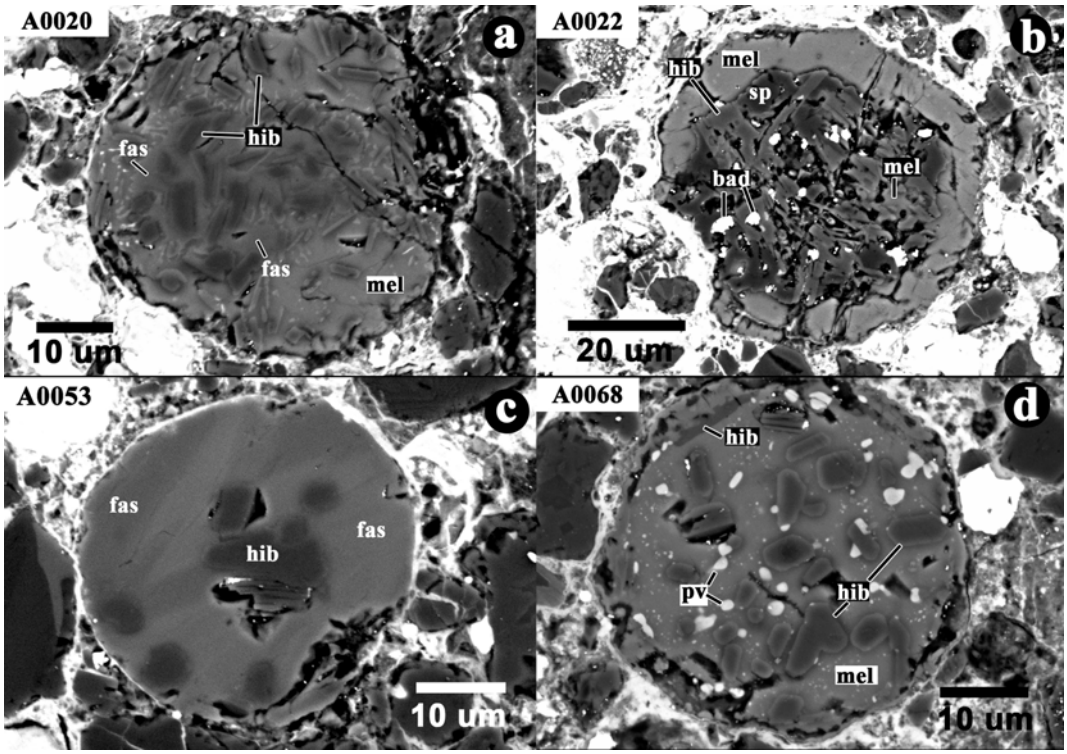

Fig. 3. BSE images of hibonite-rich CAIs in SaU 290. a) A0020 consists of a hibonite-fassaite core and a hibonite-melilite mantle. b) A0022 consists of a hibonite-spinel core and a melilite mantle. c) A fassaite-hibonite spherule (A0053) contains platy and granular crystals of hibonite. d) A0068 contains euhedral grains of hibonite and fine perovskite. hib: hibonite; fas: fassaite; mel: melilite; sp: spinel; bad: baddeleyite; pv: perovskite.

in texture to that of fassaite-anorthite-rich CAIs but has a high abundance of olivine. A few very fine spinel grains are enclosed by anorthite. No melilite grains are observed.

Aluminum-Rich Chondrules

Al-rich chondrules (ARCs) in this study are chondrules or their fragments having bulk Al_2O_3 contents higher than 10 wt% as defined by Bischoff and Keil (1984). ARCs are common in SaU 290, but less abundant than refractory inclusions. On the basis of dominant Al-rich phases, they are divided into fassaite-rich ARCs, Al-enstatite-rich ARCs, glass-rich ARCs, and anorthite-rich ARCs.

Fassaite-rich ARCs, 40–100 μm in size, are rounded or irregular in shape. They mainly consist of fassaite and olivine. Most olivine grains are rounded in shape and enclosed by fassaite grains (Figs. 8b and 8c). Spinel also occurs as fine grains or with a digested outline (Figs. 8a, 8b, and 8d). Some fassaite-rich ARCs contain mesostasis or anorthite (Figs. 8b–d). Al-enstatite exists in one fassaite-rich ARC (Fig. 8b).

Al-enstatite-rich ARCs, 70–100 μm in size, commonly consist of olivine, Al-enstatite, and fassaite. Olivine grains, rounded in shape, are included by Al-enstatite and fassaite (Fig. 9). Spinel occurs as fine-grained inclusions in Al-enstatite grains or in interstices between Al-enstatite and fassaite (Fig. 9a).

Glass-rich ARCs, 100–500 μm in size, have porphyritic or skeletal textures (Fig. 10). The porphyritic glass-rich ARCs contain olivine or fassaite phenocrysts. In the diopside-bearing porphyritic glass-rich ARC, some silica grains (~5 μm) occur in mesostasis (Fig. 10b). In the skeletal glass-rich ARCs, fassaite grains commonly occur as overgrowth phases on skeletal olivine grains (Figs. 10c). In one porphyritic glass-rich ARC, low-Ca pyroxene grains grow along euhedral porphyritic olivine grains and are enclosed by euhedral fassaite grains (Fig. 10d).

Anorthite-rich ARCs, 50–100 μm in size, commonly consist of olivine, fassaite, and anorthite. These chondrules show various petrographic features from one to another. In Fig. 11a, olivine grains form skeletal texture, and they are enclosed by fassaite and anorthite. Anorthite grains are lath-shaped. In Fig. 11b, olivine grains are barred and the interstices between olivine grains are filled by paralleled anorthite grains. Fine-grained fassaite grains in turn filled the spaces between anorthite grains. The ARC in Fig. 11c is a typical barred-olivine chondrule with the interstices filled by anorthite and fassaite.

Mineral Chemistry

Hibonite exhibits a compositional variation with respect to petrographic appearance (Table 1). Hibonite grains in

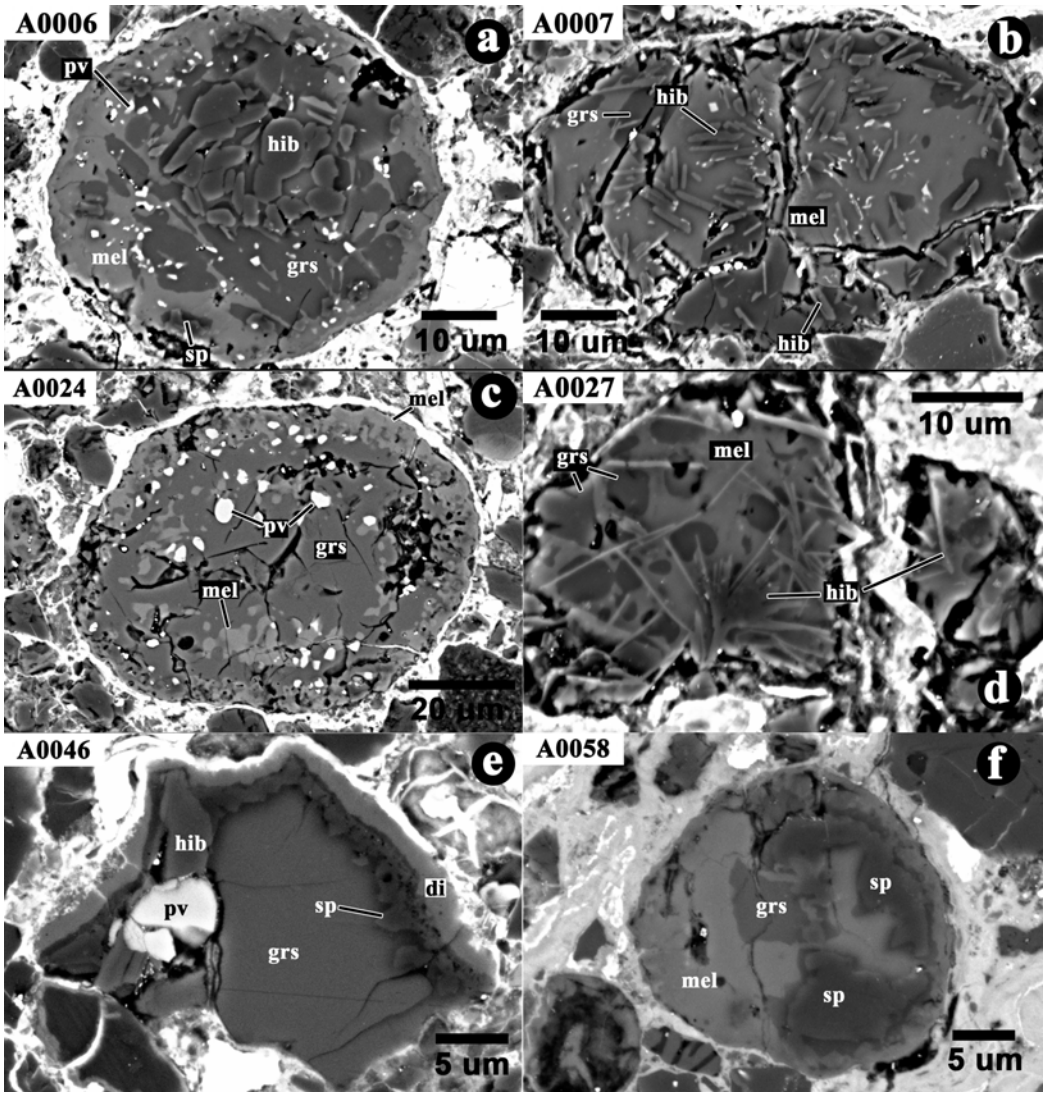

Fig. 4. BSE images of grossite-rich CAIs in SaU 290. a) A0006 has a hibonite core surrounded by grossite (grs) and melilite. b) A0007 contains hibonite needles enclosed by melilite and grossite. c) A0024 contains dominant grossite with irregular melilite and rounded perovskite grains. d) Grossite grains in A0027 are enclosed by melilite. e) A0046 has a grossite core, which was surrounded by hibonite-spinel-perovskite and diopside (di). f) A0058 consists of grossite, spinel, and melilite.

spinel-bearing inclusions have high contents of TiO_2 (5.25–5.97 wt%) and MgO (2.81–3.69 wt%) and low Al_2O_3 (78.26–81.61 wt%), whereas those in spinel-free inclusions show relatively low contents of TiO_2 (0.37–3.05 wt%) and MgO (0.62–1.35 wt%) and high Al_2O_3 (84.44–88.55 wt%). FeO contents (0.22–0.65 wt%) of hibonite in SaU 290 are similar to those in other CH chondrites (e.g., ALH 85085, Grossman et al. 1988; Kimura et al. 1993; NWA 739, Krot et al. 2006a). All hibonite grains have low concentrations (≤0.12 wt%) of Na_2O, K_2O, MnO, Cr_2O_3, and ZnO. The only exception is the hibonite grain in A0027, which has ZnO content up to 0.31 wt% and a high SiO_2 content (Table 1), probably due to contamination of surrounding phases (Fig. 4d).

Grossite grains in all CAIs are nearly pure $CaAl_4O_7$. They have low contents of FeO (0.24–0.96 wt%), similar to those in ALH 85085 (Kimura et al. 1993). Compared to hibonite, grossite is depleted in MgO (<0.68 wt%) and TiO_2 (<0.33 wt%).

Melilite is a common mineral in most CAIs of SaU 290. Representative compositions of melilite are given in Table 3. Melilite grains in grossite (or hibonite)-rich CAIs are gehlenitic and have a relatively narrow compositional variation ($Åk_1$–$Åk_{20}$), whereas most melilite grains in melilite (or fassaite)-rich CAIs are also gehlenitic but have a larger compositional variation ($Åk_4$–$Åk_{60}$) (Fig. 12). The highest Åk-content ($Åk_{60}$) was found in a relict of fassaite-bearing melilite-rich CAI A0028 (Fig. 5b). FeO contents (0.15 to 1.29 wt%) of melilite grains are similar to those in NWA 739 (Krot et al. 2006a). Most melilite grains have low Na_2O contents (<0.06 wt%) and only one data point has Na_2O content up to 0.14 wt%.

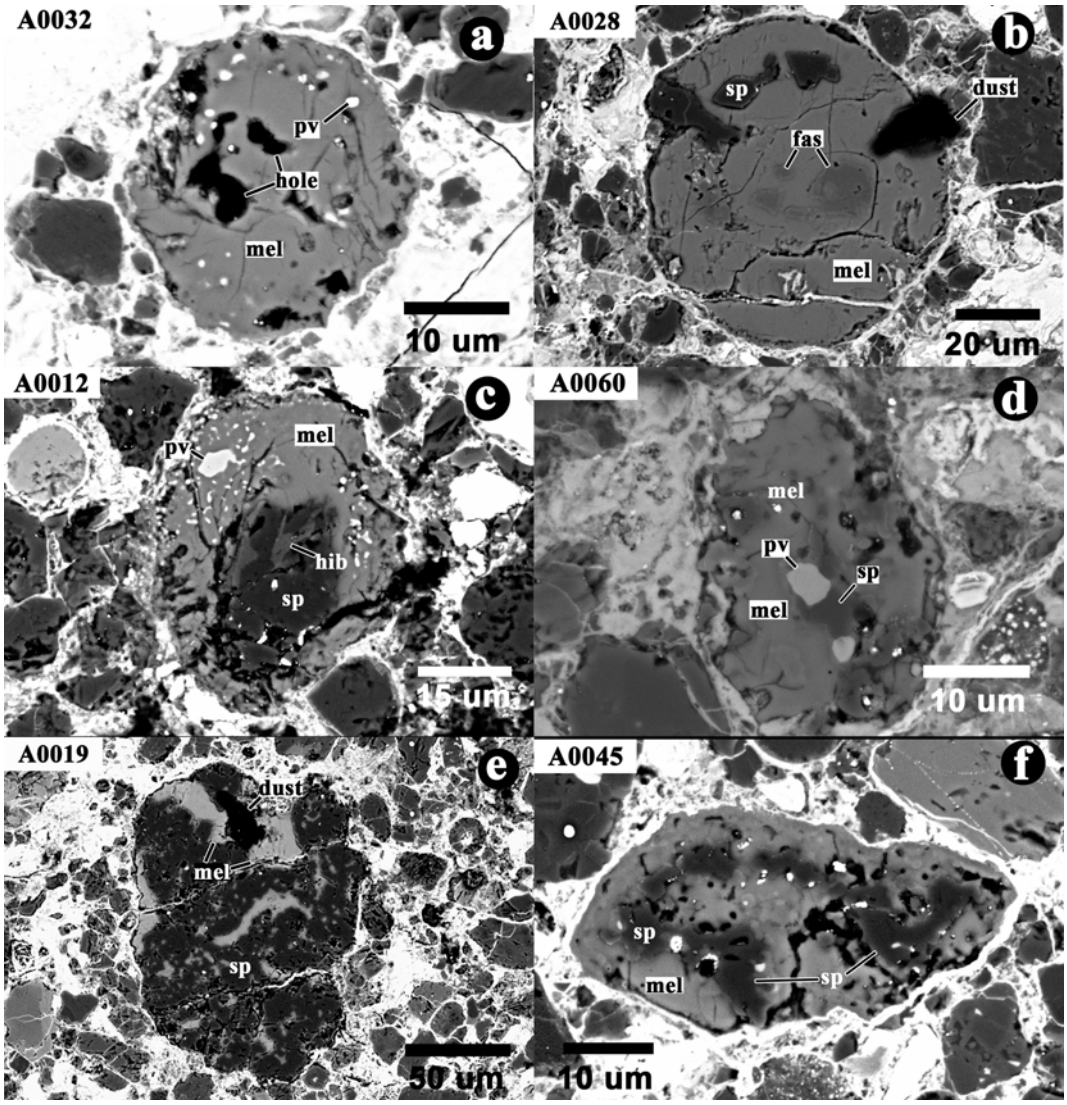

Fig. 5. BSE images of melilite-rich CAIs in SaU 290. a) A0032 is largely composed of melilite with very fine-grained perovskite. b) A0028 has a compact texture with several irregular fassaite grains included by melilite. c) A0012 has a spinel-hibonite core and a melilite-perovskite mantle. d) A0060 has a compact texture with spinel and perovskite enclosed by melilite. e) A0019 is largely composed of spinel with melilite filling interstices of spinel grains. f) A few spinel grains are enclosed by a layer of melilite.

Spinel grains in SaU 290 are nearly pure $MgAl_2O_4$. The contents of FeO, TiO_2, and Cr_2O_3 are low (0.28–0.78 wt%, 0.02–0.67 wt%, and 0.02–0.73 wt%, respectively), similar to those in other CH chondrites (Kimura et al. 1993; Krot et al. 2006a).

Most perovskite grains in SaU 290 CAIs are too small to obtain good EMPA results. Some perovskite grains (>3 μm) are nearly pure $CaTiO_3$ and contain low Al_2O_3 contents (0.83–1.20 wt%). One perovskite grain (~5 μm across) in A0046 contains 8.06 wt% Al_2O_3 and 1.21 wt% FeO. Such a high Al_2O_3 content in perovskite has not been reported from other chondrites (Brearley and Jones 1998). The two oxide grains in A0031 are too small to obtain reliable analyses (e.g., low total values varying from 89.2 to 95.3 wt%). Both of these two oxide phases have high contents of TiO_2 (38.9 wt% for ox1 and 46.7 wt% for ox2), Sc_2O_3 (12.6 wt% for ox1 and 8.5 wt% for ox2 without correcting for X-ray interferences of Sc-K_α and Ca-K_β peaks), ZrO_2 (2.3 wt% for ox1 and 2.5 wt% for ox2), and Y_2O_3 (2.9 wt% for ox1 and 1.4 wt% for ox2). Al_2O_3, CaO, and Cr_2O_3 contents in ox1 (10.8, 7.7, and 1.7 wt%, respectively) are higher than those in ox2 (7.0, 3.9, and 1.1 wt%, respectively). In addition, both oxide phases contain minor Na_2O (1.0 and 1.4 wt%). More detailed work is needed to identify these two oxide phases.

Most pyroxene grains in refractory inclusions from SaU 290 are high-Ca pyroxene. Al_2O_3 contents in these high-Ca pyroxene grains show a wide compositional variation from 1.15 to 50.67 wt%. Those in hibonite-fassaite inclusions (A0020, A0053, and A0065) are characterized with high Al_2O_3 (23.99–50.67 wt%); some grains in the cores of other

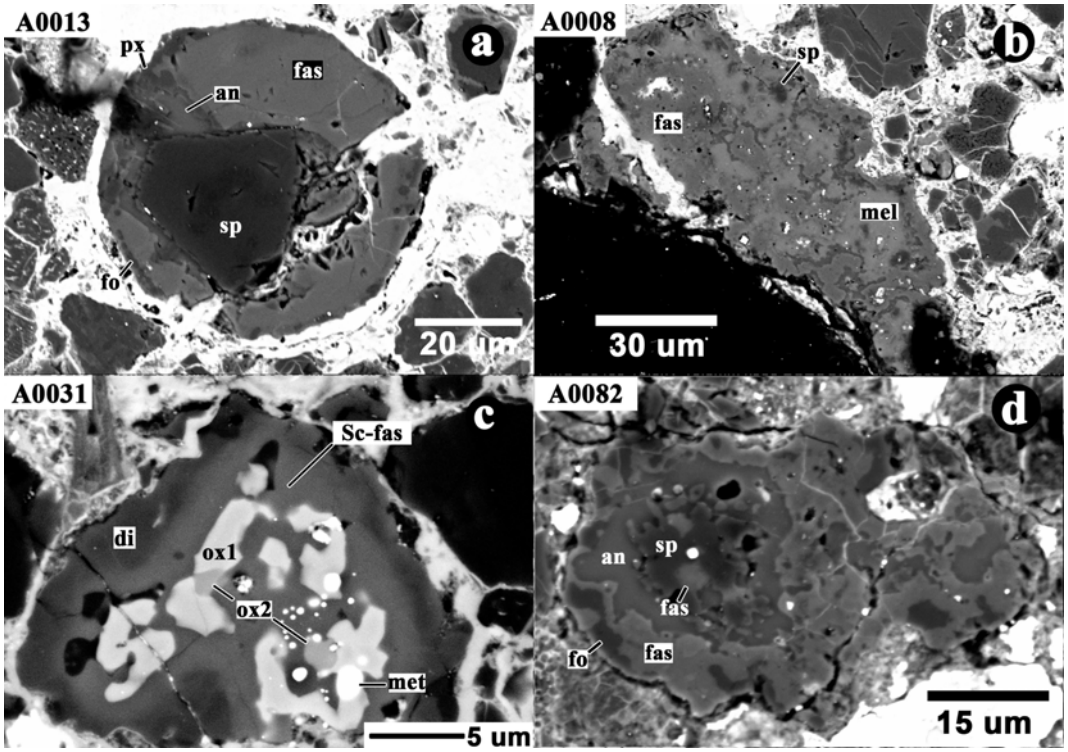

Fig. 6. BSE images of fassaite-rich CAIs in SaU 290. a) A0013 contains a spinel grain enclosed by fassaite. b) A0008 contains melilite, fassaite, and spinel with the former replaced by the latter two phases. c) A0031 contains two Sc-,Ti-,Y-, and Zr-rich oxide phases (ox1 and ox2) which are surrounded by Sc-rich fassaite (Sc-fas) and diopside. d) A0082 is composed mainly of anorthite and fassaite with a discontinuous rim of forsterite (fo).

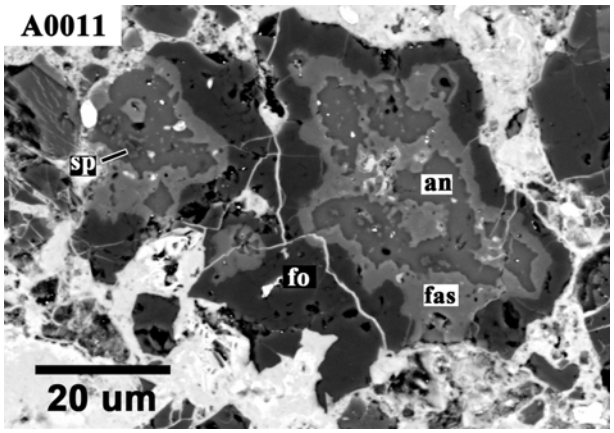

Fig. 7. BSE image of the amoeboid olivine aggregate (A0011).

refractory inclusions (e.g., A0028 and A0082) also have high Al_2O_3 contents (17.33–19.34 wt%). The highest Al_2O_3 content (50.67 wt%) was found in the core of a hibonite-rich CAI A0020 (Fig. 3a). Most high-Ca pyroxene grains in refractory inclusions contain <2 wt% TiO_2; however, a few grains in cores of refractory inclusions (e.g., A0028 and A0082) have high TiO_2 contents (up to 10.62 wt%), similar to those in other CH chondrites (e.g., ALH 85085, Kimura et al. 1993; NWA 739, Krot et al. 2006a).

Most pyroxene grains in ARCs are also high-Ca pyroxene. However, high-Ca pyroxene grains in ARCs contain higher Cr_2O_3 (0.02–1.31 wt%) and MnO (up to 0.09 wt%) than those in refractory inclusions (Fig. 13). The compositional ranges of Al_2O_3 (5.7–20.31 wt%) and TiO_2 (0.09–3.49 wt%) are smaller in ARCs than in refractory inclusions. Most high-Ca pyroxene grains in fassaite-rich ARCs have higher Al_2O_3 contents (17.66–20.31 wt%) than those in glass-rich ARCs (7.81–15 wt%), Al-enstatite-rich ARCs (10.8–14.21 wt%), and anorthite-rich ARCs (5.7–9.89 wt%). Low-Ca pyroxene grains in fassaite-rich and Al-enstatite-rich ARCs have high Al_2O_3 contents (12.07–13.93 wt%) and low TiO_2 contents (0.44–0.62 wt%), whereas the low-Ca pyroxene grain in a glass-rich ARC (ch056) has a low Al_2O_3 content (3.04 wt%).

Olivine grains in the AOA are nearly pure forsterite ($Fa_{0.6–1.42}$) and contain minor Cr_2O_3 (0.25–0.28 wt%) and MnO (0.08–0.33 wt%). Olivine grains from glass-rich, fassaite-rich, and anorthite-rich ARCs are generally forsterite ($Fa_{0.42–2.78}$, $Fa_{0.82–3.66}$, and $Fa_{0.61–3.16}$, respectively), slightly Fe-richer than those in the AOA (Fig. 14); olivine grains in Al-enstatite-rich ARCs (<$Fa_{1.13}$) have fayalite components comparable to those in the AOA. Cr_2O_3 contents of olivine in glass-rich, fassaite-rich, and anorthite-rich ARCs are slightly higher than those in the AOA (Fig. 14).

Anorthite grains in most refractory inclusions and ARCs have compositions near pure $CaAl_2Si_2O_8$ (Fig. 6). Na_2O and

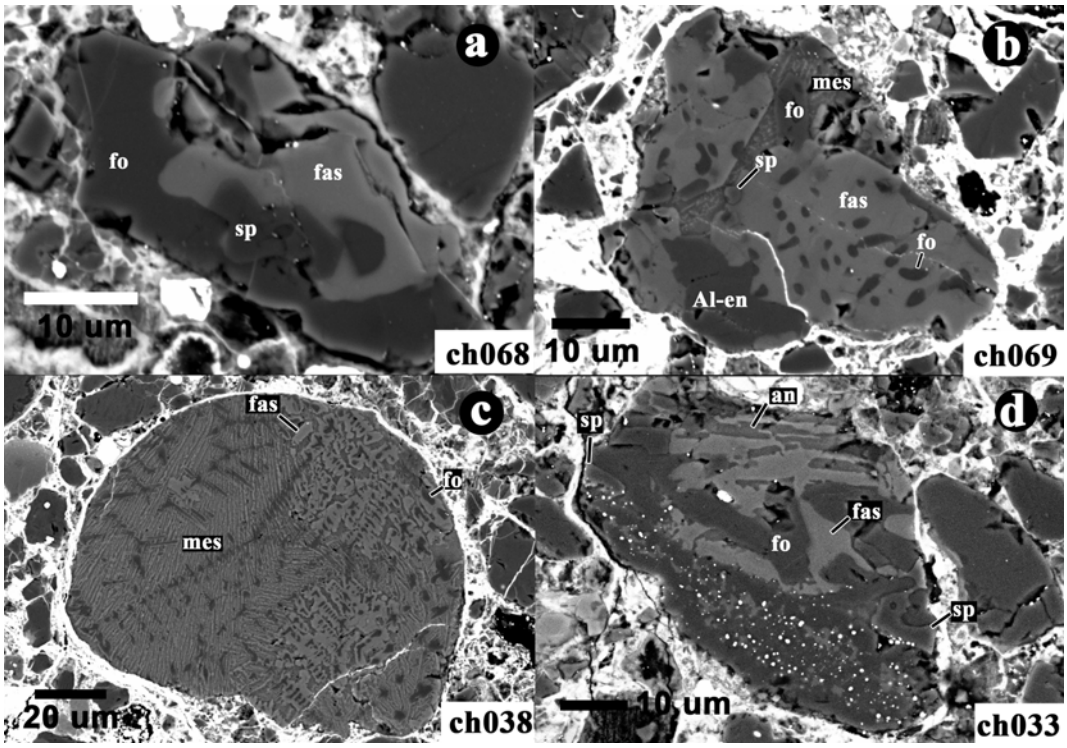

Fig. 8. BSE images of fassaite-rich ARCs in SaU 290. a) A fragment (ch068) containing forsterite and fassaite. b) The chondrule fragment (ch069) consists of forsterite, fassaite, Al-enstatite (Al-en), mesostasis (mes), and spinel. c) The chondrule (ch038) consists of skeletal forsterite grains overgrown by fassaite and mesostasis. d) The chondrule fragment (ch033) consists of forsterite, fassaite, anorthite, and spinel.

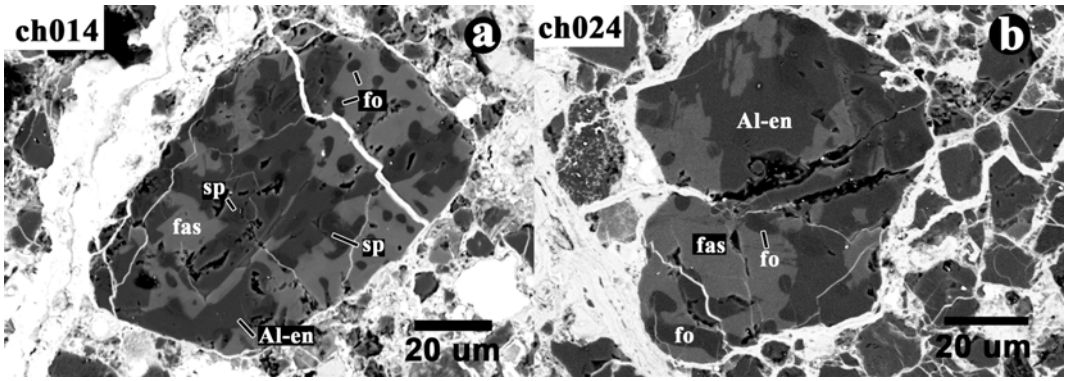

Fig. 9. BSE images of Al-enstatite-rich ARCs in SaU 290.

K_2O contents are very low (<0.1 wt%); the only exception is plagioclase in A0013, which contains 0.15 wt% Na_2O. However, anorthite grains in some fassaite-anorthite-rich inclusions commonly contain several weight percents of FeO + MgO, which could be contaminated results due to their small sizes. Most glasses (mesostasis) in ARCs are rich in SiO_2, Al_2O_3 and CaO (>54 wt%, 19.12–22.79 wt% and 11.07–16.55 wt%, respectively). The glass in Fig. 8b has an unusual low SiO_2 content (36.17 wt%) and a high Al_2O_3 (37.96 wt%) (Point 18 in Table 6). MgO contents (2.50–12.31 wt%) are higher than FeO contents (0.31–1.21 wt%). Compared to anorthite grains, glasses contain high Na_2O (0.06–2.52 wt%, averaging at 0.61 wt%).

Bulk Chemistry of Refractory Inclusions and ARCs

Bulk compositions of CAIs, AOA, ARCs, and some type-I chondrules from SaU 290 are plotted on a phase diagram that represents a projection from spinel onto the plane Al_2O_3-Ca_2SiO_4-Mg_2SiO_4 (Fig. 15). The bulk compositions of CAIs, in order of volatility (hibonite-rich → grossite-rich → melilite±spinel-rich → fassaite-spinel-rich → fassaite-anorthite-rich), generally follow the equilibrium condensation trajectory, but are systematically rich in Al_2O_3. Bulk composition of the AOA plots on a region between Al-diopside, anorthite, and forsterite and to the left of the anorthite-forsterite thermal divide (Fig. 15). The bulk

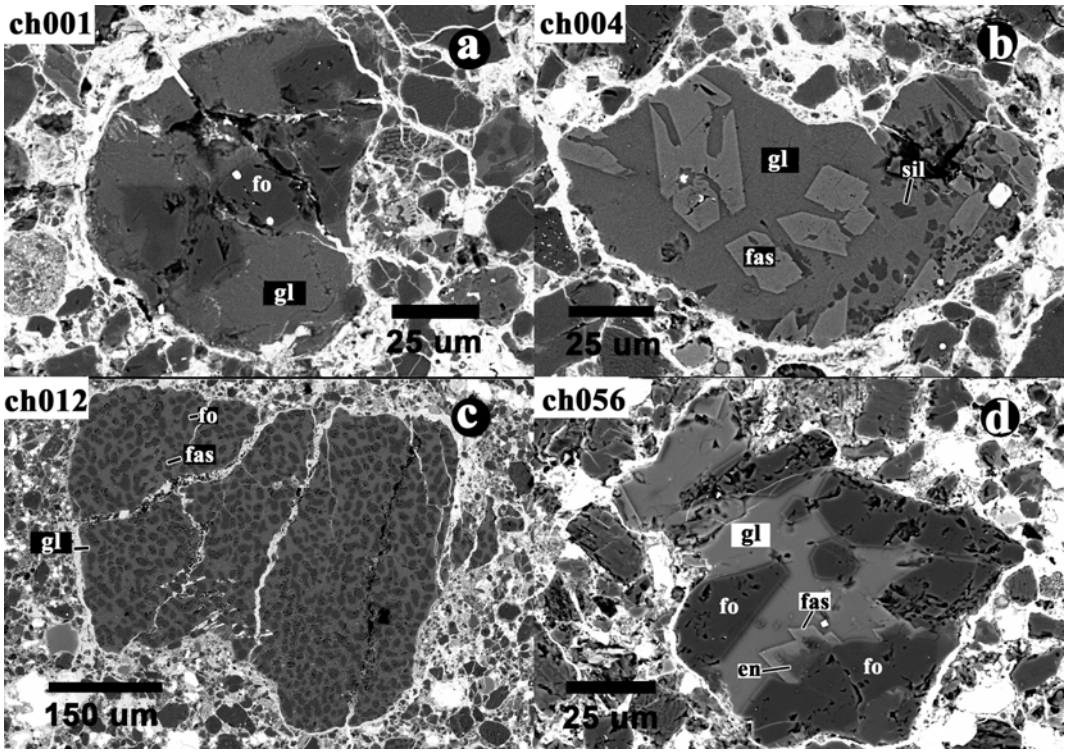

Fig. 10. BSE images of glass-rich ARCs in SaU 290. a) The chondrule (ch001) contains forsterite phenocrysts enclosed by glass. b) The chondrule fragment (ch004) contains a few fassaite phenocrysts and some fine-grained silica (sil) grains. c) The chondrule (ch012) has a skeletal texture with rounded forsterite grains included by glass. d) The chondrule fragment (ch056) mainly consists of euhedral forsterite grains and mesostasis (glass).

compositions of ARCs plot on the field between fassaite-spinel-rich CAIs and type-I chondrules (Fig. 15). Fassaite-rich ARCs plot near the field occupied by the AOA (Fig. 15). Bulk compositions of glass-rich and Al-enstatite-rich ARCs plot to the right of the thermal divide; the compositional ranges of the former are larger than those of the latter. Bulk compositions of anorthite-rich ARCs generally plot along the thermal divide (Fig. 15).

DISCUSSION

Pristine Nature of Refractory Inclusions in SaU 290 and Comparison to Those in other Chondrites

Although most metal grains in SaU 290 have been weathered, refractory inclusions show no evidence of terrestrial weathering that commonly result in formation of clay minerals. This fact suggests that refractory inclusions retain their chemical and mineralogical features in nebular and/or parent body settings. Both regular (e.g., rounded) and irregular refractory inclusions in SaU 290 have sharp interfaces with surrounding objects. This indicates that thermal metamorphism on its parent body did not severely affect refractory inclusions. In addition, no low-temperature alteration minerals (e.g., nepheline, sodalite, grossular, wollastonite, hedenbergite, ferrous olivine, andradite, carbonates, and phyllosilicates) were observed in refractory inclusions, indicating low-temperature secondary alteration processes have minimal effects on the refractory inclusions. Therefore, refractory inclusions in SaU 290 are pristine and mainly record high-temperature processes in the early solar nebular setting.

Similar to other CH chondrites, apparent sizes of CAIs in SaU 290 are relatively small. CAIs in SaU 290 have a size distribution (10–151 μm, with a mean of ~40 μm) slightly larger than those from ALH 85085 (<5–107 μm, the mean size is 31 μm) (Grossman et al. 1988) but smaller than those in Acfer 182 (up to 450 μm) and NWA 739 (a mean size of ~70 μm) (Bischoff et al. 1993; Krot et al. 2006a). In general, CH CAIs are smaller than those in other chondrite groups (e.g., CV, CR, and CO), which commonly have a mean size up to several hundred microns, even to a centimeter level (Scott 2007). The size distribution of CAIs in different chondrites is probably caused by various growing rates of CAIS controlled by physical-chemical conditions, although a strong sorting mechanism in the early solar nebular setting has also been proposed (Weisberg et al. 1988).

The types of CAIs in SaU 290 are similar to those in other CH chondrites, but distinct from those of other groups of carbonaceous chondrites. Although grossite-bearing and hibonite-bearing CAIs are less abundant in SaU 290 (27%) than in other CH chondrites (e.g., ~40% grossite-bearing

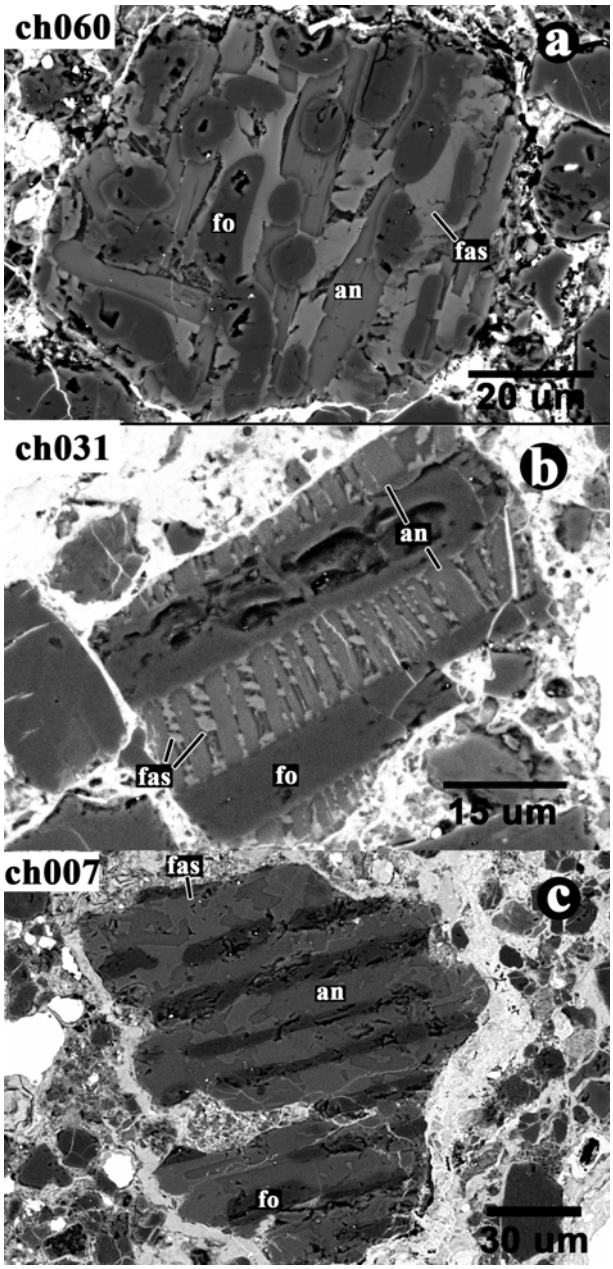

Fig. 11. BSE images of olivine-diopside-anorthite ARCs in SaU 290. a) The chondrule fragment (ch060) has a skeletal texture with rounded forsterite grains overgrown by fassaite and anorthite. b) The chondrule fragment (ch031) consists of forsterite, anorthite, and fassaite. c) The chondrule fragment (ch007) has a barred texture with anorthite and fassaite occurring in the interstices of forsterite.

CAIs in ALH 85085, Kimura et al. 1993; 16% hibonite-rich + 26% grossite-rich CAIs in NWA 739, Krot et al. 2006a), they are much more abundant than in other groups of carbonaceous chondrites (Krot et al. 2002b). In CM chondrites, the dominant type of CAIs is spinel-pyroxene inclusions, while the hibonite-bearing inclusions are less abundant (e.g., 8% in Queen Alexandra Range [QUE] 97990, Rubin 2007). Melilite-rich inclusions are very rare in CM chondrites (Simon et al. 2006; Rubin 2007). CV chondrites are characterized by type-B inclusions but contain very rare hibonite, or grossite-rich inclusions. In CO chondrites, most CAIs are spinel-pyroxene and melilite varieties and the abundance of hibonite and grossite-bearing inclusions are very low (Russell et al. 1998). Most CAIs in CR chondrites are melilite-rich and spinel-rich inclusions. Hibonite-bearing and grossite-bearing inclusions are very rare (Krot et al. 2002b). CB_b chondrites are dominated by pyroxene-rich inclusions (Krot et al. 2001). Generally, hibonite-bearing and grossite-bearing inclusions are common in CH chondrites compared to those in other groups of chondrites. This indicates a highly refractory nature of CAIs in CH chondrites and reflects a distinct population of refractory inclusions among different carbonaceous chondrites.

The different population of refractory inclusions was probably due to various formation regions or formation episodes with different physical-chemical conditions. If refractory inclusions were formed in different nebular regions, the formation regions could have different dust/gas ratios, cooling rates, and peck heating temperatures. For instance, the more refractory inclusions are probably related to higher peak heating temperatures, which require that their formation region is closer to the center of the protoplanetary disk. Alternatively, refractory inclusions could have formed in a common region and then were dispersed to the whole solar nebula by some processes, e.g., outer migration by an X-wind (Shu et al. 1996), turbulent diffusion (Cuzzi et al. 2003), and large-scale fluid motions in a marginally gravitationally unstable disk (Boss 2007). The refractory nature of refractory inclusions in SaU 290, compared to those in other groups of chondrites, requires higher peak heating temperatures. If refractory inclusions were formed in different nebular regions, the formation region of refractory inclusions in SaU 290 is probably closer to the center of the protoplanetary disk than those of other groups of chondrites. If CAIs were formed in a common region of the solar nebula, those in SaU 290 were probably formed earlier than those of other groups of chondrites. Isotopic analyses are much needed to gain additional constrains on the formation of CAIs in SaU 290. Krot et al. (2008) inferred that some more refractory inclusions (composed mainly of hibonite, grossite, Al-rich pyroxene, perovskite, and gehlenitic melilite) in one CH chondrite and a CH/CB-like chondrite formed before less refractory inclusions on the basis of their Al-Mg isotopic system and oxygen isotopic compositions. Recently, Krot and Nagashima (2009) infer that ^{16}O-poor CAIs in CH and CB chondrites were melted during the impact that formed chondrules, several Myr after CAI formation.

AOAs are rare in CH chondrites. Krot et al. (2004b) found 15 AOAs in NWA 739 and NWA 770 and compared them with those counterparts in other carbonaceous chondrites. They found that AOAs in all primitive carbonaceous chondrites are similar in mineral assemblages and that AOAs containing relict melilite-rich CAIs are only present in CH chondrites (Krot et al. 2006a). AOAs are very

Table 1. Representative EMPA results of hibonite in SaU 290 CAIs (wt%).

	Associated with spinel					Not associated with spinel					
	A0063	A0022	A0046	A0012	A0020	A0006	A0053	A0007	A0068	A0068	A0027
SiO_2	0.30	1.38	0.64	1.30	0.17	0.11	0.16	1.30	0.48	b.d.	2.49
TiO_2	5.78	5.97	5.34	5.25	1.03	2.95	1.95	2.53	2.10	0.23	0.37
Al_2O_3	81.61	78.44	80.69	78.26	88.45	86.41	87.67	84.53	86.62	85.36	84.44
Cr_2O_3	0.02	0.02	0.07	0.04	b.d.	b.d.	b.d.	0.03	0.02	0.03	b.d.
FeO	0.57	0.55	0.51	0.41	0.48	0.22	0.39	0.43	0.34	0.54	0.65
MnO	b.d.	b.d.	0.08	b.d.	b.d.	0.02	b.d.	b.d.	b.d.	0.07	0.03
MgO	3.69	3.19	2.81	2.88	0.92	1.30	0.98	1.27	1.09	0.42	1.03
ZnO	b.d.	b.d.	0.10	0.07	0.02	0.05	0.05	0.07	0.12	n.a.	0.31
CaO	8.15	9.81	8.80	8.67	8.71	8.54	8.32	10.18	8.77	13.19	9.52
Na_2O	0.02	b.d.	b.d.	0.02	b.d.	b.d.	0.02	b.d.	b.d.	0.10	0.07
K_2O	b.d.	b.d.	b.d.	b.d.	b.d.	b.d.	0.02	b.d	0.02	0.04	b.d.
Total	100.1	99.36	99.04	96.9	99.78	99.6	99.56	100.3	99.56	100*	98.91

*Recalculated by subtracting the contribution of Si, Al, and Ca from surrounding melilite. b.d. = Below detection limit; n.a. = Not analyzed.

Table 2. Representative EMPA results of grossite in SaU 290 CAIs (wt%).

	A0024	A0063	A0006	A0058	A0046	A0007	A0067	A0027
SiO_2	0.13	0.04	0.32	0.18	0.11	0.88	0.06	0.03
TiO_2	0.09	0.10	0.21	0.31	0.17	0.07	0.06	0.33
Al_2O_3	77.57	78.08	76.70	76.55	77.33	75.67	77.63	77.43
Cr_2O_3	b.d.	b.d.	b.d.	b.d.	0.02	0.02	b.d.	0.03
FeO	0.40	0.52	0.24	0.45	0.28	0.47	0.89	0.52
MnO	b.d.	b.d.	0.02	b.d.	b.d.	0.02	b.d.	b.d.
MgO	0.08	0.07	0.11	0.10	0.03	0.46	0.04	0.04
ZnO	0.06	0.04	b.d.	0.04	0.05	0.06	b.d.	0.02
CaO	21.45	20.91	21.49	21.74	21.64	21.17	20.91	21.64
Na_2O	b.d.	b.d.	0.02	b.d.	0.07	0.02	b.d.	0.04
K_2O	b.d.	b.d.	b.d.	b.d.	b.d.	b.d.	b.d.	b.d.
Total	99.78	99.76	99.11	99.37	99.7	98.84	99.59	100.1

b.d. = Below detection limit.

Table 3. Representative EMPA results of melilite in SaU 290 CAIs (wt%).

	Grs (or hib)-rich CAIs						Mel (or fas)-rich CAIs					
SiO_2	24.55	22.79	24.32	21.97	24.14	23.47	33.23	23.42	36.00	29.46	28.73	23.12
TiO_2	b.d.	0.02	0.02	0.74	b.d.	0.04	0.03	0.08	0.05	b.d.	0.04	0.15
Al_2O_3	32.88	35.62	32.94	35.18	33.48	34.52	19.02	34.07	13.95	24.65	25.66	34.14
Cr_2O_3	0.02	0.04	b.d.	b.d.	0.04	b.d.	0.03	0.02	b.d.	0.03	0.04	b.d.
FeO	0.80	0.78	0.59	0.28	0.82	0.42	0.25	0.91	0.15	0.47	0.49	0.45
MnO	0.03	b.d.	b.d.	b.d.	0.03	b.d.	b.d.	0.02	b.d.	b.d.	b.d.	b.d.
MgO	1.92	0.18	1.35	0.26	3.17	0.85	7.01	1.02	8.38	4.30	4.20	0.71
ZnO	0.14	0.09	0.10	0.05	0.08	0.02	0.11	0.12	0.18	b.d.	0.03	0.08
CaO	39.83	41.13	40.11	39.97	37.97	39.91	39.71	38.25	40.23	39.80	39.95	40.04
Na_2O	b.d.	b.d.	b.d.	0.02	0.04	0.02	b.d.	0.04	b.d.	0.02	b.d.	b.d.
K_2O	0.02	b.d.	b.d.	b.d.	b.d.	b.d.	b.d.	b.d.	b.d.	b.d.	b.d.	b.d.
Total	100.2	100.7	99.43	98.47	99.77	99.25	99.39	97.95	98.94	98.73	99.14	98.69
Åk	12.9	1.2	9.4	1.8	19.3	5.9	48.3	7.0	60.3	30.6	29.3	5.0

b.d. = Below detection limit.

rare in SaU 290 and no melilite grains or melilite-rich CAIs were observed in the AOAs.

High-Temperature Nebular Processes Recorded by CAIs in SaU 290

On the basis of calculated mineral condensation temperatures by Lodders (2003), lack of relatively more refractory corundum and less refractory forsterite and enstatite suggests that most CAI minerals in SaU 290 (except A0013) would have formed in the temperature range of 1659–1347 K from a solar gas or of 1647–1339 K from a photospheric composition.

Based on petrographic textures, Kimura et al. (1993) suggest that most CAIs in ALH 85085 have crystallized from refractory melt droplets or experienced late re-crystallization.

Table 4. Representative EMPA results of pyroxene in refractory inclusions and Al-rich chondrules (wt%).

	A0021	A0023	A0008	A0053	A0053	A0046	A0013	A0013	A0005	A0028	A0009	A0011
SiO_2	42.98	49.88	50.11	33.30	34.09	48.48	47.24	54.95	54.14	43.89	35.71	55.00
TiO_2	0.71	0.93	0.72	0.50	7.56	0.24	1.00	0.67	0.22	2.04	13.65	0.16
Al_2O_3	26.82	8.64	7.60	36.38	26.62	3.62	12.07	2.20	3.22	17.33	17.14	1.15
Cr_2O_3	0.06	0.05	0.09	0.05	0.07	0.11	b.d.	0.76	0.05	0.03	0.12	b.d.
FeO	3.83	0.48	0.64	0.66	0.54	4.15	0.39	1.89	0.74	0.20	1.57	0.6
MnO	0.04	b.d.	b.d.	b.d.	b.d.	b.d.	b.d.	0.15	b.d.	b.d.	0.03	b.d.
MgO	3.39	14.88	16.53	3.49	5.26	16.54	15.03	36.15	18.86	10.82	8.15	18.95
ZnO	0.05	0.05	0.07	0.14	b.d.	b.d.	0.05	0.03	b.d.	0.05	0.13	0.04
CaO	19.10	25.38	24.01	25.18	24.95	22.92	23.62	3.65	23.02	24.81	23.90	24.39
Na_2O	0.17	0.02	b.d.	b.d.	0.02	0.16	0.02	0.06	b.d.	b.d.	b.d.	b.d.
K_2O	0.03	b.d.	b.d.	b.d.	b.d.	0.02	b.d.	0.02	b.d.	0.02	b.d.	b.d.
Total	97.18	100.3	99.77	99.7	99.11	96.24	99.42	100.5	100.3	99.19	100.4	100.3
	A0011	A0082	A0082	ch004	ch012	ch007	ch056	ch031	ch014	ch014	ch038	ch068
SiO_2	50.13	35.72	49.86	51.46	45.54	51.18	49.22	52.81	51.50	47.29	44.68	43.46
TiO_2	0.57	8.38	0.95	1.33	1.91	1.93	1.09	3.04	0.44	0.09	1.00	2.54
Al_2O_3	9.11	19.22	6.02	7.81	15.00	5.70	13.46	9.46	13.16	14.21	18.60	18.02
Cr_2O_3	0.03	0.09	0.11	0.63	1.14	0.40	0.81	0.97	0.08	0.04	0.02	0.15
FeO	1.23	0.60	0.75	0.62	0.96	0.34	0.41	1.37	0.43	0.54	0.26	0.65
MnO	b.d.	b.d.	b.d.	0.02	0.03	0.02	0.05	b.d.	b.d.	b.d.	b.d.	b.d.
MgO	14.45	8.93	17.72	17.55	13.99	17.85	14.59	10.49	32.36	15.64	10.88	11.18
ZnO	0.03	n.a.	n.a.	0.02	0.12	0.08	0.06	0.08	0.09	0.11	0.08	n.a.
CaO	23.78	24.64	24.07	20.36	20.79	21.63	19.92	22.05	1.41	21.12	24.41	23.91
Na_2O	0.03	0.08	0.02	b.d.	0.02	0.07	0.05	b.d.	b.d.	b.d.	b.d.	b.d.
K_2O	b.d.	b.d.	b.d.	b.d.	b.d.	0.02	b.d.	b.d.	b.d.	b.d.	b.d.	b.d.
Total	99.36	97.66	99.5	99.8	99.5	99.22	99.66	100.3	99.47	99.04	99.93	99.91

b.d. = Below detection limit; n.a. = Not analyzed.

Table 5. Representative EMPA results of olivine in AOA and ARCs (wt%).

	A0011	ch001	ch007	ch012	ch014	ch033	ch060	ch056	ch031	ch031
SiO_2	42.66	42.58	42.21	42.28	42.93	42.10	42.04	42.44	42.02	42.96
TiO_2	0.08	0.08	0.08	0.10	b.d.	0.33	0.05	0.08	0.03	0.41
Al_2O_3	0.03	0.10	0.10	0.09	0.29	0.35	0.08	b.d.	0.06	1.90
Cr_2O_3	0.28	0.25	0.15	0.40	0.08	0.29	0.41	0.39	0.33	0.05
FeO	0.60	0.94	0.62	3.13	0.48	2.73	2.85	1.10	1.56	0.63
MnO	0.08	0.02	b.d.	0.02	b.d.	0.02	b.d.	0.04	b.d.	b.d.
MgO	55.13	55.55	55.85	53.45	55.82	53.13	54.11	55.43	55.07	51.39
ZnO	0.11	0.03	b.d.	0.06	0.04	0.02	0.07	0.06	0.06	b.d.
CaO	0.16	0.37	0.23	0.27	0.17	0.21	0.20	0.22	0.27	2.37
Na_2O	b.d.	b.d.	0.02	b.d.	b.d.	b.d.	b.d.	0.04	b.d.	b.d.
K_2O	b.d.	b.d.	b.d.	b.d.	b.d.	b.d.	b.d.	b.d.	b.d.	b.d.
Total	99.13	99.92	99.26	99.8	99.81	99.18	99.81	99.8	99.4	99.71

b.d. = Below detection limit.

In NWA 739, Krot et al. (2006a) observed that most CAIs, spherical or oval in shape, are porous and suggested a nebular condensation origin. In SaU 290, most spherical CAIs have igneous textures and are less porous. They could have crystallized from refractory melt droplets that probably formed due to high dust/gas ratio (Krot et al. 2004b) or formed from subsequent melting of pre-existing condensates. Irregular CAIs and some spherical or oval CAIs without igneous textures commonly have a layered texture. They might have directly condensed from the solar nebula. One CAI (A0020) could be the product of evaporation of refractory melt.

Most spinel-free and hibonite-bearing CAIs have an igneous texture whereas those hibonite-spinel-bearing inclusions commonly have a layered texture. The textural difference implies their different formation processes. The igneous texture indicates that the spinel-free and hibonite-bearing inclusions could have crystallized from refractory melt droplets or experienced subsequent melting of pre-existing condensates. On the other hand, hibonite-spinel-bearing inclusions probably represent gas-solid condensates of the solar nebula. Similar explanation has been proposed to interpret formation of spinel-, hibonite-rich inclusions from CM2 carbonaceous chondrites (Simon et al. 2006). The

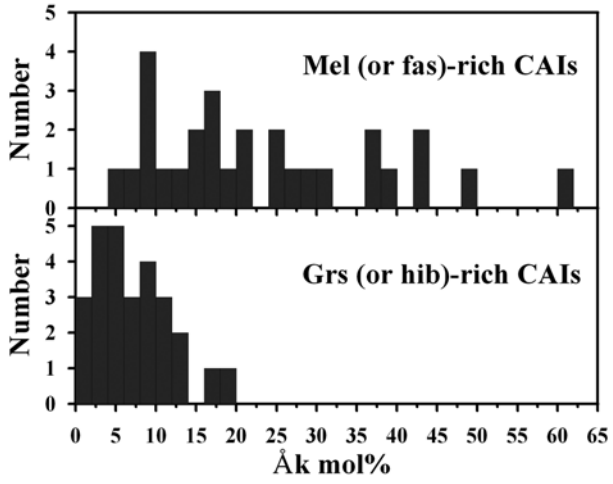

Fig. 12. Åkermanite component distribution of melilite in different CAIs of SaU 290.

texture of hibonite-spinel-bearing inclusions, however, is in conflict with equilibrium condensation sequence (melilite prior to spinel) from a solar gas (Yoneda and Grossman 1995). Simon et al. (2006) suggested kinetic inhibition of melilite relative to spinel. They stated that it should be easier for spinel than for melilite to form from hibonite due to similar crystal structures between spinel and hibonite. It is possible that formation of spinel prior to melilite in hibonite-spinel-bearing inclusions of SaU 290 could be due to the kinetic inhibition of melilite condensation relative to spinel; however, it is not clear whether spinel formed from hibonite by gas-solid reaction because spinel and hibonite have an intergrowth texture rather than a replacement texture (Figs. 3b and 5c).

Mineral assemblages and chemistry of hibonite in SaU 290 also provide some clues to understand the formation of hibonite-spinel-bearing inclusions. Hibonite coexisting with spinel has high contents of TiO_2 and MgO than that not coexisting with spinel (Table 1). The difference could be caused by varying chemistry of the system in which hibonite-bearing CAIs formed. Based on calculation results with CWPI (Condensation With Partial Isolation) code (Petaev et al. 2003), Krot et al. (2004a) proposed that condensation of a Ca-depleted system (depleted in Ca by 84.4% or more) can account for the mineralogy and texture of hibonite- and spinel-rich inclusions. The condensation sequence is generally consistent with petrography and mineral assemblage of hibonite-spinel CAIs. Krot et al. (2004a) proposed that Ti_3O_5, a theoretic phase in calculation result, and hibonite probably condense into a single phase. This explanation is consistent with high TiO_2 contents in hibonite grains that are associated with spinel. However, the calculated Ti content (0.2 wt%) in hibonite is significantly lower than the values observed in SaU 290 (up to 6 wt%, Table 1). Nevertheless, as Krot et al. (2004a) noted, the question where and how such fractionated systems might be created remains unsolved.

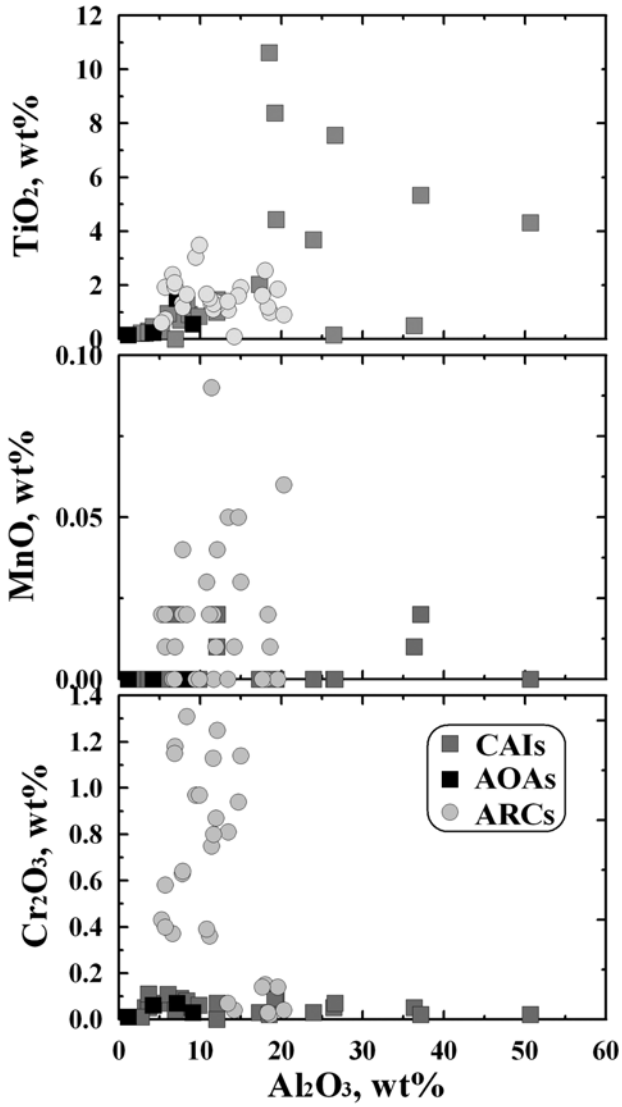

Fig. 13. Concentrations of Al_2O_3 versus TiO_2, MnO, and Cr_2O_3 in high-Ca pyroxenes of CAIs, AOA, and ARCs from SaU 290.

We noted that hibonite-spinel-bearing inclusions in SaU 290 have a layered texture whereas most spinel-free, hibonite-bearing inclusions have an igneous or a re-crystallized texture. One possibility exists that the latter formed from melting of inclusions containing Ti,Mg-rich hibonite (even with influx of other components). When re-crystallization starts, Ti is carried by perovskite or fassaite rather than hibonite, and Mg is partitioned into fassaite or melilite.

Although grossite-rich CAIs in SaU 290 are not as porous as those observed in NWA 739, they are also probably condensates of the solar nebula. In most grossite-rich CAIs, grossite is replaced by melilite. This replacement is consistent with their condensation sequence (Petaev et al. 2003). Krot et al. (2006a) suggested that replacement of grossite by melilite could be explained by the reaction of grossite with gaseous Ca and SiO:

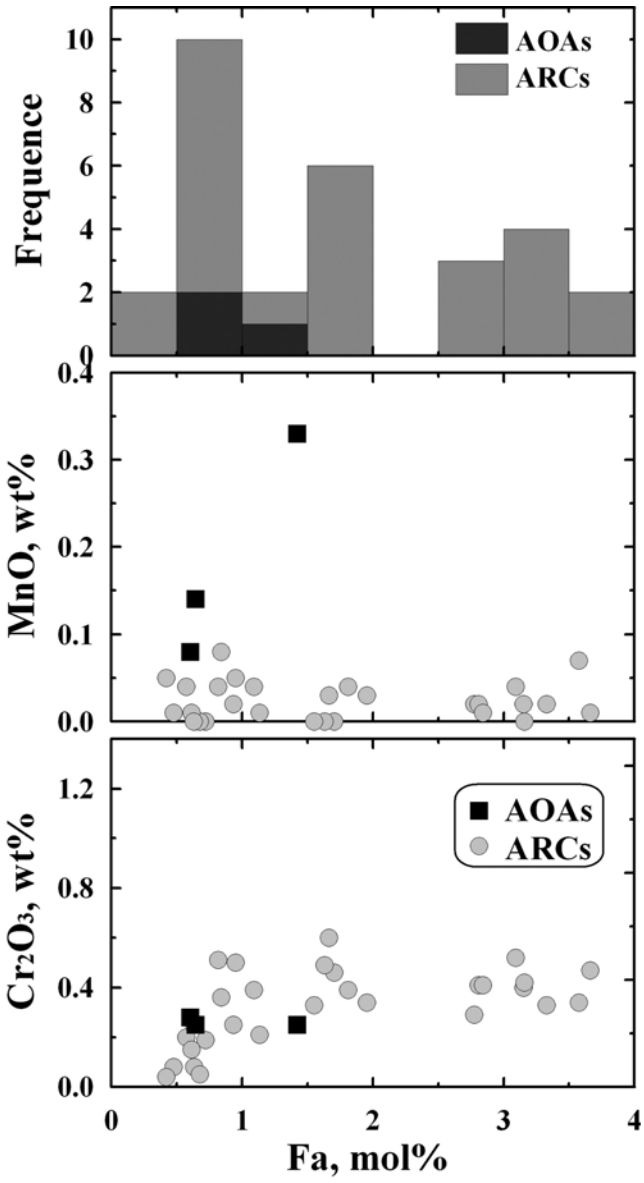

Fig. 14. Histogram of fayalite contents (in mol%) and concentrations (in wt%) of MnO and Cr_2O_3 versus Fa contents in olivine of AOA (black symbols) and ARCs (grey and open symbols) from SaU 290.

$$CaAl_4O_7 + 3Ca(g) + 2SiO(g) + 5H_2O(g) = 2Ca_2Al_2SiO_7 + 5H_2(g) \quad (1)$$

They also suggested that this reaction would be out of equilibrium for the relative high Åk components (>$Åk_5$). This interpretation is generally suitable to the replacement texture in most grossite-rich CAIs in SaU 290.

Most melilite-rich and fassaite±spinel-rich CAIs (e.g., A0012, A0045, A0008, and A0031) in SaU 290 could be high-temperature condensates. However, some CAIs could have experienced later re-melting and re-crystallization. For instance, the inclusion A0028 has a rounded shape and a compact texture. Furthermore, fassaite in this inclusion appears with a digested outline. This may indicate a replacement of fassaite by melilite, reflecting a reaction of $CaAl_2SiO_6$ component with gaseous Ca:

$$CaAl_2SiO_6 + Ca(g) + H_2O(g) = Ca_2Al_2SiO_7 + H_2(g) \quad (2)$$

The high Åk (30–60) components of melilite in this inclusion also support this suggestion because the high MgO contents of melilite are very likely inherited from fassaite. In addition, the fact that enstatite and forsterite are missing in this inclusion suggests that the replacement represent a melting event that is not related to the chondrule-forming heating event.

Some melilite grains are replaced by diopside and spinel (e.g., in A0008). This replacement could be expressed by the reaction of $Ca_2Al_2SiO_7$ with gaseous SiO and Mg:

$$Ca_2Al_2SiO_7 + 3SiO(g) + 3Mg(g) + 6H_2O(g) = 2CaMgSi_2O_6 + MgAl_2O_4 + 6H_2(g) \quad (3)$$

In addition, one fassaite-anorthite-rich inclusion (A0082) contains a relict spinel-fassaite assemblage. This texture indicates a complex formation history, possibly involving a replacement of spinel and fassaite by anorthite and forsterite as suggested by Krot et al. (2004a):

$$2MgAl_2O_4 + CaAl_2SiO_6 + 6SiO(g) + 2Ca(g) + 2H_2O(g) = 3CaAl_2Si_2O_6 + Mg_2SiO_4 + 2H_2(g) \quad (4)$$

The inclusion A0020 probably represents evaporation product of pre-existing refractory solid. Major observations supporting this suggestion include: 1) this inclusion has a core-mantle texture; 2) the core has a digested outline; 3) the mantle contains hibonite and melilite while the core contains hibonite and fassaite. On the basis of equilibrium condensation from a solar gas, Mg-poor melilite solid solution (1416–1390 K) is more refractory than Al,Ti-rich clino-pyroxene (1399–1322 K) (Krot et al. 2004a). Thus, the mantle of A0020 appears to be more refractory than the core. When the precursor of A0020 experienced a very high temperature (higher than the melting point of fassaite and lower than that of hibonite), some Mg and Si in the outer fassaite vaporized and caused the formation of melilite. Trace-element geochemical study of melilite and fassaite is needed to verify this explanation.

Origin of the AOA (A0011) and Relationship with CAIs

The AOA in SaU 290 is irregularly shaped and has a layered texture similar to those in other carbonaceous chondrites (Adelaide, Krot et al. 2004c; NWA 739, Krot et al. 2006a), indicating formation as aggregates of gas-solid nebular condensates (Krot et al. 2004c). Possible reaction involved is replacement of spinel by anorthite and diopside:

$$MgAl_2O_4 + 2Ca(g) + 4SiO(g) + 6H_2O(g) = CaAl_2Si_2O_8 + MgCaSi_2O_6 + 6H_2(g) \quad (5)$$

The fact that the AOA in SaU 290 has similar mineralogy and texture to some fassaite-anorthite-rich inclusions

Table 6. Representative EMPA results of anorthite and glass in refractory inclusions and ARCs (wt%).

	A0011	A0013	ARC anorthite				ARC glasses				
SiO_2	43.23	46.69	44.53	44.02	45.11	45.67	56.38	62.66	36.17	57.84	57.07
TiO_2	0.11	0.06	0.05	0.11	b.d.	0.14	0.87	0.28	0.19	0.26	0.41
Al_2O_3	35.75	33.71	34.19	34.16	34.37	33.22	19.12	20.71	37.96	21.76	22.15
Cr_2O_3	0.04	0.02	b.d.	b.d.	b.d.	b.d.	0.46	0.14	1.35	0.32	0.11
FeO	0.72	0.36	0.29	0.32	0.32	0.67	0.51	0.31	0.85	0.39	1.21
MnO	b.d.	0.04	b.d.	b.d.	b.d.	b.d.	0.09	0.06	0.03	0.03	0.03
MgO	0.34	1.13	0.41	0.78	0.44	0.78	4.57	2.50	12.31	4.52	4.99
ZnO	0.03	0.04	0.05	0.11	0.03	0.05	0.02	0.02	b.d.	0.04	0.08
CaO	18.92	17.39	19.62	19.58	19.46	19.37	14.64	11.93	11.07	13.77	14.06
Na_2O	0.03	0.15	0.10	0.07	b.d.	b.d.	2.52	0.91	0.15	0.44	0.11
K_2O	b.d.	b.d.	b.d.	b.d.	b.d.	b.d.	0.07	b.d.	b.d.	b.d.	0.02
Total	99.17	99.59	99.24	99.15	99.73	99.9	99.25	99.52	100.1	99.37	100.2

b.d. = Below detection limit.

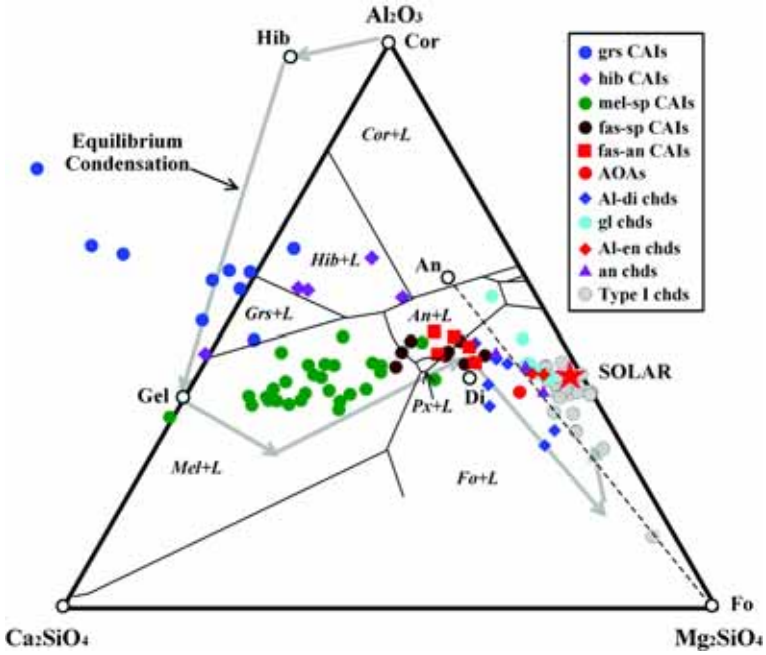

Fig. 15. Bulk compositions of CAIs, AOA, ARCs, and type-I chondrules from SaU 290 projected from spinel onto the plane Al_2O_3-Ca_2SiO_4-Mg_2SiO_4. The thick grey vectors show calculated trajectory for bulk condensed solids during equilibrium condensation (after MacPherson and Huss 2000). Dashed line connecting anorthite and forsterite is a thermal divide. The star represents the solar composition.

suggests that the AOA is genetically related with fassaite-anorthite-rich inclusions.

Origin of Al-Rich Chondrules and Possible Relationships with Refractory Inclusions

Al-diopside-rich ARCs are relatively dominant in SaU 290, followed by glass-rich, plagioclase-rich, and Al-enstatite-rich ARCs, similar to other CH chondrites (e.g., NWA 739; Krot et al. 2006a). In comparison, plagioclase-rich ARCs are the dominant type in most CV and CR chondrites (Krot et al. 2002a; Krot and Keil 2002). The difference suggests that CH, CR, and CV ARCs formed from precursor materials that originated in different ARC-forming regions (Krot and Keil 2002). In addition, ARCs in SaU 290 do not contain low-temperature alteration phases (e.g., nepheline, sodalite, and ferrous olivine), suggesting that they did not experience severe secondary low-temperature alteration after their formation. On the contrast, nepheline, a typical low-temperature alteration mineral, commonly exists in ARCs of CV chondrites and ordinary chondrites (Krot et al. 2002a; MacPherson and Huss 2005).

From analyses of ARCs in ordinary chondrites, MacPherson and Huss (2005) proposed that bulk composition is the main controlling factor on ARC types. Dynamic crystallization experiments by Tronche et al. (2007) also indicate that bulk composition is a main controlling factor in terms of mineralogy and texture. In NWA 739, Krot et al. (2006a) observed that Al-diopside-rich and plagioclase-rich ARCs plot on different sides of the anorthite-forsterite

thermal divide of the phase diagram. Al-diopside-rich ARCs and glass-rich ARCs also plot on different sides of the forsterite-anorthite thermal divide (Fig. 15). Plagioclase-rich ARCs in ordinary chondrites plot on the An+L region (Fig. 9b in MacPherson and Huss 2005) and those in carbonaceous chondrites plot on the right side of the anorthite-forsterite thermal divide (Krot et al. 2006a). Plagioclase-rich ARCs in SaU 290 plot out of the An + L region and along the thermal divide (Fig. 15). This difference implies other controlling factors exist (Tronche et al. 2007).

We note that in SaU 290, the AOA, some fassaite-anorthite-rich inclusions, one Al-diopside-rich ARC (Fig. 8d), and anorthite-rich ARCs have a similar mineral assemblage (consisting of fassaite, anorthite, and forsterite) but show distinctly different textures. The layered texture of the AOA and some fassaite-anorthite-rich inclusions implies a condensation origin rather than a crystallization origin from melts. All of the ARCs have a crystallization texture. If we assume that AOAs, fassaite-anorthite-rich inclusions, and ARCs formed directly in the solar nebula, this distinction is probably related to different total pressures and/or dust/gas ratios (Krot et al. 2004b and references therein). It is possible that the local nebular setting where/when CAIs and AOAs formed has low total pressure and/or low dust/gas ratio and gas-solid condensation is preferred; whereas the local nebular setting where/when ARCs formed has high total pressure and/or dust/gas ratio and an Al-rich melt droplet is easy to form, resulting in a crystallization texture. If ARCs formed due to mixing between ferromagnesian chondrules and CAI materials, they could represent a heating event in chondrule-forming region, based on the general formation sequence from CAIs to chondrules. In addition, textural difference of some ARCs with similar chemical compositions is probably controlled by cooling rates of precursor melts, because constituting phases have a large variation of grain size and shape among different chondrules. This explanation is consistent with synthetic experimental results by Tronche et al. (2007).

We note that anorthite and Al-enstatite do not co-exist in ARCs of SaU 290. Bulk compositions of these ARCs are variable from one to another. But Al-enstatite-rich and anorthite-rich ARCs do not show significant difference in bulk compositions (Fig. 15). For instance, the difference of most major element compositions (e.g., Al_2O_3, SiO_2, CaO, and FeO) between the Al-enstatite-rich ARC in Fig. 9a and the anorthite-rich ARC in Fig. 11a is less than 1 wt%. This may suggest that bulk composition is not the key controlling factor to the decoupling presence of Al-enstatite and anorthite. Rubin (2004) suggested that the occurrence of Al-enstatite must be due mainly to the kinetic failure of anorthite nucleation, which resulted in rapid crystal growth with the pyroxene stability field. In SaU 290, petrographic textures of Al-enstatite-rich/-bearing ARCs (Figs. 8b and 9) are indeed distinctly different from those of anorthite-rich ARCs (Fig. 11). In Al-enstatite-rich ARCs, Al-enstatite grains are anhedral in shape; however, anorthite grains in anorthite-rich ARCs are lath-shaped. This petrographic difference probably results from a kinetic effect during crystallization of ARCs.

Precursors of ARCs have been suggested as mixtures of CAI materials and ferromagnesian chondrules (Russell et al. 2000; Srinivasan et al. 2000; Krot et al. 2002a; MacPherson and Huss 2005; Guan et al. 2006; Hezel et al. 2006; Hezel and Palme 2007). This suggestion is supported by the following observations: (1) bulk compositions of ARCs generally plot between ferromagnesian chondrules and CAI materials (e.g., Krot et al. 2004a); (2) many ARCs have textures similar to those of normal chondrules and contain relict CAI fragments (Krot et al. 2006a); (3) some heterogeneous ARCs consist of Ca,Al-rich portions and Fe,Mg-rich portions (Acfer 094, Krot et al. 2004a); (4) oxygen isotopic compositions of ARCs commonly overlap ferromagnesian chondrules and extending to ^{16}O-rich compositions (Krot et al. 2006b). In this study, bulk compositions of most ARCs in SaU 290 also plot on the region between CAIs and ferromagnesian chondrules (Fig. 15), supporting the suggestion that precursor materials of these ARCs were derived from mixing of CAIs and ferromagnesian chondrules. The presence of irregular spinel grains (Figs. 8b, 8d, and 9a) that probably are of relict origin in some ARCs also support this conclusion, but no large CAI-like fragments were observed in ARCs. ARCs in SaU 290 do not consist of two chemically and mineralogically distinct portions as observed in Acfer 094 (Krot et al. 2004a). The homogeneous textures of ARCs in SaU 290 might indicate relatively high-degree melting during chondrule formation. We note that one glass-rich ARC (Fig. 10b) contains some grains of silica. Silica is absent in CAIs and rare in most ferromagnesian chondrules and ARCs in CH chondrites (Hezel et al. 2003). The occurrence of silica may indicate that this glass-rich ARC is not a simple mixture of CAI and ferromagnesian chondrules, consistent with previous investigations (Russell et al. 2000; Guan et al. 2006).

Rubin (2004) suggested that a Ca-Al-rich chondrule (G7) could have formed by melting of an AOA precursor. The main evidence is that proportions of component phases in some AOAs from Yamato-81020 CO3 chondrite match those of the bulk composition of G7. Krot et al. (2002a) argued against this suggestion based on differences of mineral chemistry of relict CAIs, existence of low-Ca pyroxene, oxygen isotopic compositions of forsterite in plagioclase-rich chondrules and AOAs and their petrographic textures from reduced CV chondrites. In this study, it is difficult to infer possible genetic relationship between AOA and ARCs on the basis of mineralogies and bulk compositions only because AOA and ARCs (especially plagioclase-rich ARCs) are relatively rare in SaU 290. Further oxygen isotope analyses of CAIs, AOAs, and ARCs will help to understand the origin of ARCs.

Acknowledgments—The sample used in this study is provided by Rainer Bartoschewitz. The first author thanks Prof. Chengdong Liu and Mr. Guolin Guo for the assistance of electron microprobe analyses at East China Institute of Technology. The authors would express their gratitude to Drs. Sasha Krot and D. C. Hezel for their helpful reviews and to Associate Editor Edward R. D. Scott for editorial efforts. This study is supported by National Natural Science Foundation of China (Grant nos. 10621303, 40703015, and 40773046), the Minor Planet Foundation of China, and the Open Foundation of State Key Laboratory for Mineral Deposits Research, Nanjing University (Grant Nos. 13–7–6 and 14–8–6).

Editorial Handling—Dr. Edward Scott

REFERENCES

Bartoschewitz R., Appel P., Mader B., Park J., Nagao K., Okazaki R., Kusakabe M., Krähenbühl U., and Prudencio M. I. 2005. Sayh Al Uhaymir 290—A new CH3 chondrite (abstract #5079). *Meteoritics & Planetary Science* 40:A18.

Beckett J. R., Connolly H. C., and Ebel D. S. 2006. Chemical processes in igneous calcium-aluminum-rich inclusions: A mostly CMAS view of melting and crystallization. In *Meteorites and the early solar system II*, edited by Lauretta D. S. and McSween H. Y. Jr. Tucson: The University of Arizona. pp. 399–429.

Bischoff A. and Keil K. 1984. Al-rich objects in ordinary chondrites: Related origin of carbonaceous and ordinary chondrites and their constituents. *Geochimica et Cosmochimica Acta* 48:693–709.

Bischoff A., Palme H., Schultz L., Weber D., Weber H. W., and Spettel B. 1993. Acfer 182 and paired samples, an iron-rich carbonaceous chondrite: Similarities with ALH 85085 and relationship to CR chondrites. *Geochimica et Cosmochimica Acta* 57:2631–2648.

Boss A. P. 2007. Evolution of the solar nebula. VIII. Spatial and temporal heterogeneity of short-lived radioisotopes and stable oxygen isotopes. *The Astrophysical Journal* 660:1707–1714.

Brearley A. J. and Jones R. H. 1998. Chondritic meteorites. In *Planetary materials*, edited by Papike J. J. Washington, DC: Mineralogical Society of America. pp. 3.1–3.398.

Cuzzi J. N., Davis S. S., and Dobrovolskis A. R. 2003. Blowing in the wind. II. Creation and redistribution of refractory inclusions in a turbulent protoplanetary nebula. *Icarus* 166:385–402.

Guan Y. B., Huss G. R., Leshin L. A., MacPherson G. J., and McKeegan K. D. 2006. Oxygen isotope and ^{26}Al-^{26}Mg systematics of aluminum-rich chondrules from unequilibrated enstatite chondrites. *Meteoritics & Planetary Science* 41:33–47.

Grossman J. N., Rubin A. E., and MacPherson G. J. 1988. ALH 85085: A unique volatile-poor carbonaceous chondrite with possible implications for nebular fractionation processes. *Earth and Planetary Science Letters* 91:33–54.

Hezel D. C. 2007. A model for calculating the errors of 2D bulk analysis relative to the true 3D bulk composition of an object, with application to chondrules. *Computers & Geosciences* 33: 1162–1175.

Hezel D. C. and Palme H. 2007. The conditions of chondrule formation, Part I: Closed system. *Geochimica et Cosmochimica Acta* 71:4092–4107.

Hezel D. C., Palme H., Brenker F. E., Nasdala L. 2003. Evidence for fractional condensation and reprocessing at high temperatures in CH chondrites. *Meteoritics & Planetary Science* 38:1199–1215.

Hezel D. C., Palme H., Nasdala L., and Brenker F. E. 2006. Origin of SiO_2-rich components in ordinary chondrites. *Geochimica et Cosmochimica Acta* 70:1548–1564.

Ireland T. R., Fahey A. J., and Zinner E. K. 1991. Hibonite-bearing microspherules: A new type of refractory inclusions with large isotopic anomalies. *Geochimica et Cosmochimica Acta* 55:367–379.

Kimura M., El Goresy A., Palme H., and Zinner E. 1993. Ca,Al-rich inclusions in the unique chondrite ALH 85085: Petrology, chemistry, and isotopic compositions. *Geochimica et Cosmochimica Acta* 57:2329–2359.

Krot A. N. and Keil K. 2002. Anorthite-rich chondrules in CR and CH carbonaceous chondrites: Genetic link between calcium-aluminum-rich inclusions and ferromagnesian chondrules. *Meteoritics & Planetary Science* 37:91–111.

Krot A. N., McKeegan K. D., Russell S. S., Meibom A., Weisberg M. K., Zipfel J., Krot T. V., Fagan T. J., and Keil K. 2001. Refractory calcium-aluminum-rich inclusions and aluminum-diopside-rich chondrules in the metal-rich chondrites Hammadah al Hamra 237 and Queeen Alexandra Range 94411. *Meteoritics & Planetary Science* 36:1189–1216.

Krot A. N., Hutcheon I. D., and Keil K. 2002a. Plagioclase-rich chondrules in the reduced CV chondrites: Evidence for complex formation history and genetic links between calcium-aluminum-rich inclusions and ferromagnesian chondrules. *Meteoritics & Planetary Science* 37:155–182.

Krot A. N., Meibom A., Weisberg M. K., Keil K. 2002b. The CR chondrite clan: Implications for early solar system process. *Meteoritics & Planetary Science* 37:1451–1490.

Krot A. N., Keil K., Goodrich C. A., and Scott E. R. D. 2003. Classification of meteorites. 83–128. In *Meteorites, comets, and planets*, edited by Davis A. M. Treatise on Geochemistry, vol. 1. Elsevier-Pergamon, Oxford.

Krot A. N., Fagan T. J., Keil K., McKeegan K. D., Sahijpal S., Hutcheon I. D., Petaev M. I., and Yurimoto H. 2004a. Ca,Al-rich inclusions, amoeboid olivine aggregates, and Al-rich chondrules from the unique carbonaceous chondrite Acfer 094: I. Mineralogy and petrology. *Geochimica et Cosmochimica Acta* 68:2167–2184.

Krot A. N., Libourel G., Goodrich C. A., and Petaev M. I. 2004b. Silica-rich igneous rims around magnesian chondrules in CR carbonaceous chondrites: Evidence for condensation origin from fractionated nebular gas. *Meteoritics & Planetary Science* 39: 1931–1955.

Krot A. N., Petaev M. I., Russell S. S., Itoh S., Fagan T. J., Yurimoto H., Chizmadia L., Weisberg M. K., Komatsu M., Ulyanov A. A., and Keil K. 2004c. Amoeboid olivine aggregates and related objects in carbonaceous chondrites: Records of nebular and asteroid processes. *Chemie der Erde* 64:185–239.

Krot A. N., Petaev M. I., and Keil K. 2006a. Mineralogy and petrology of Al-rich objects and amoeboid olivine aggregates in the CH carbonaceous chondrite Northwest Africa 739. *Chemie der Erde* 66:57–76.

Krot A. N., Libourel G., and Chaussidon M. 2006b. Oxygen isotope compositions of chondrules in CR chondrites. *Geochimica et Cosmochimica Acta* 70:767–779.

Krot A. N., Nagashima K., Bizzarro M., Huss G. R., Davis A. M., Meyer B. S., and Ulyanov A. A. 2008. Multiple generations of refractory inclusions in the metal-rich carbonaceous chondrites Acfer 182/214 and Isheyevo. *The Astrophysical Journal* 672: 713–721.

Krot A. N. and Nagashima K. 2009. Isotopically uniform, ^{16}O-depleted CAIs in metal-rich carbonaceous chondrites (abstract #1036). 40th Lunar and Planetary Science Conference. CD-ROM.

Lodders K. 2003. Solar system abundances and condensation temperatures of the elements. *The Astrophysical Journal* 591: 1220–1247.

MacPherson G. J. 2003. Calcium-aluminum-rich inclusions in chondritic meteorites. 201–246. In *Meteorites, comets, and planets*, edited by Davis A. M. Treatise on Geochemistry, vol. 1. Elsevier-Pergamon, Oxford.

MacPherson G. J. and Huss G. R. 2000. Convergent evolution of CAIs and chondrules: Evidence from bulk compositions and a cosmochemical phase diagram (abstract #1796). 31st Lunar and Planetary Science Conference. CD-ROM.

MacPherson G. J. and Huss G. R. 2005. Petrogenesis of Al-rich chondrules: Evidence from bulk compositions and phase equilibria. *Geochimica et Cosmochimica Acta* 69:3099–3127.

MacPherson G. J., Davis A. M., and Grossman J. N. 1989. Refractory inclusions in the unique chondrite ALH 85085. *Meteoritics* 24: 297.

Murty S. V. S., Mahajan R. R., and Bartoschewitz R. 2007. Nitrogen in Sayh al Uhaymir 290. *Meteoritics & Planetary Science* 42: A113–A113.

Park J., Okazaki R., Nagao K., and Bartoschewitz R. 2005. Noble gas study of new enstatite SaU 290 with high solar gases (abstract #1632). 36th Lunar and Planetary Science Conference. CD-ROM.

Petaev M. I., Wood J. A., Meibom A., Krot A. N., and Keil K. 2003. The ZONMET thermodynamic and kinetic model of metal condensation. *Geochimica et Cosmochimica Acta* 67:1737–1751.

Rubin A. E. 2004. Aluminian low-Ca pyroxene in a Ca-Al-rich chondrule from the Semarkona meteorite. *American Mineralogist* 89:867–872.

Rubin A. E. 2007. Petrography of refractory inclusions in CM2.6 QUE 97990 and the origin of melilite-free spinel inclusions in CM chondrites. *Meteoritics & Planetary Science* 42:1711–1726.

Russell S. S., Huss G. R., Fahey A. J., Greenwood R. C., Hutchison R., and Wasserburg G. J. 1998. An isotopic and petrologic study of calcium-aluminum-rich inclusions from CO3 meteorites. *Geochimica et Cosmochimica Acta* 62:689–714.

Russell S. S., MacPherson G. J., Leshin L. A., and McKeegan K. D. 2000. ^{16}O enrichments in aluminum-rich chondrules from ordinary chondrites. *Earth and Planetary Science Letters* 184: 57–74.

Sahijpal S., McKeegan K. D., Krot A. N., Weber D., and Ulyanov A. A. 1999. Oxygen isotopic compositions of calcium–aluminum-rich inclusions from the CH chondrites, Acfer 182 and PAT 91546 (abstract). *Meteoritics & Planetary Science* 34:A101.

Scott E. R. D. 2007. Chondrites and the protoplanetary disk. *Annual Review of Earth and Planetary Sciences* 35:577–620.

Shu F. H., Shang H., and Lee T. 1996. Toward an astrophysical theory of chondrites. *Science* 271:1545–1552.

Simon S. B., Grossman L., Hutcheon I. D., Phinney D. L., Weber P. K., and Fallon S. J. 2006. Formation of spinel-, hibonite-rich inclusions found in CM2 carbonaceous chondrites. *American Mineralogist* 91:1675–1687.

Srinivasan G., Huss G. R., and Wasserburg G. J. 2000. A petrographic, chemical, and isotopic study of calcium-aluminum-rich inclusions and aluminum-rich chondrules from the Axtell (CV3) chondrite. *Meteoritics & Planetary Science* 35:1333–1354.

Tronche E. J., Hewins R. H., and MacPherson G. J. 2007. Formation conditions of aluminum-rich chondrules. *Geochimica et Cosmochimica Acta* 71:3361–3381.

Weber D., Zinner E., and Bischoff A. 1995. Trace element abundances and magnesium, calcium, and titanium isotopic compositions of grossite-containing inclusions from the carbonaceous chondrite Acfer 182. *Geochimica et Cosmochimica Acta* 59:803–823.

Weisberg M. K., Prinz M., and Nehru C. E. 1988. Petrology of ALH 85085: A chondrite with unique characteristics. *Earth and Planetary Science Letters* 91:19–32.

Yoneda S. and Grossman L. 1995. Condensation of CaO-MgO-Al_2O_3-SiO_2 liquids from cosmic gases. *Geochimica et Cosmochimica Acta* 59:3413–3444.